

A Final Report Submitted to the
U.S. Department of Energy
Nuclear Engineering Education Research (NEER) Program

By the

University of Florida
Gainesville, Florida 32611

For a project entitled

***Advances in Photon and Neutron Skeletal Dosimetry
Through NMR Microscopy***

DE-FG07-99ID13764

Wesley Bolch, Principal Investigator
Edward Dugan, Co-Principal Investigator
Department of Nuclear and Radiological Engineering

Benjamin Inglis, Co-Investigator
Department of Neuroscience
Center for Structural Biology, UF Brain Institute

James E. Turner, Consultant
Oak Ridge National Laboratory

November 2002

Research Goals

The long-term goals of this project are to: (1) develop detailed 3D models of electron and charged particle transport within trabecular bone taken from various skeletal sites, subject ages, and both sexes, and (2) to extend current Reference Man skeletal dosimetry models to more clinically relevant patient populations.

1. NMR microscopy and radiation transport techniques

Detailed descriptions of our methodology for NMR microscopy of trabecular bone are given in the Appendices A-C; they are only briefly discussed here. For NMR imaging experiments that use intact marrow as the NMR signal source, only physical sectioning of the excised sample is required. For the marrow-free samples, the trabecular bone sections are first immersed and suspended within a circulating solution of 5.25% sodium hypochlorite for 2-4 hours. The samples are then rinsed in hot water and re-immersed in a new solution. This process is repeated up to four times depending on the size of the sample. Visual inspection is used to determine the number of repetitions needed. To ensure that water completely fills all marrow cavities, each sample is placed in a container filled with Gd-doped water under vacuum. While still immersed, the sample is placed in a smaller container filled with Gd-doped water. This container is sealed and taken to the Advanced Magnetic Resonance Imaging and Spectroscopy (AMRIS) Facility of the University of Florida Brain Institute for NMR microscopy.

A Bruker 20-cm wide bore Avance Imaging Spectrometer, operating at a 200 MHz proton resonance (4.7 T magnetic field strength) was used to obtain all NMR images in these studies. This system is fitted with a microimaging accessory, consisting of 3-axes magnetic field gradients, with a 22 Gauss cm⁻¹ maximum gradient amplitude in all three orthogonal directions. A 35-mm diameter quadrature birdcage coil of length 45 mm was used in order to obtain the best signal to noise ratio (SNR). For all imaging sessions, a conventional 3D spin-echo pulse sequence was used to obtain fully three-dimensional images of the samples. Fields of view are typically 4.5 cm x 2.25 cm x 2.25 cm with matrix dimensions of 512 x 256 x 256. The resulting spatial resolution of the 3D images is thus 88 µm x 88 µm x 88 µm. Smaller voxel dimensions have been achieved at UF (~ 50 µm) but at the cost of increased imaging time.

Image processing steps include (1) visual inspection of the images (to note image artifacts attributable to air bubbles, sample misalignment, or inadequate marrow digestion), (2) selection of an optimal threshold within the gray-level histogram, and (3) image filtering. A binary image is thus produced in which voxels of bone and marrow are seen within the image. An interior region-of-interest (ROI) is selected for coupling to EGS4. Electrons are permitted to begin their random paths in either the trabecular marrow space (TMS), trabecular bone volume (TBV), or trabecular bone endosteum (TBE), where the latter is defined as the region of the marrow space 10 µm from the surface of a bone voxel (*I*). If the electron leaves the ROI, it is reintroduced within a replicate copy of the image. In what is termed the infinite trabecular-region transport model, this process of particle reintroduction is continued until the full initial energy of the electron is deposited. This technique thus recreates the current assumptions made in the Reference Man skeletal model. A second approach made in our research is to develop a macrostructural transport model in which the physical size and dimensions of the trabecular spongiosa are additionally modeled, as well as the thickness of the cortex of cortical bone. A comparison of these two models is given below in Section 8. Marrow cellularity is addressed in Section 7.

2. Assessment of minimum voxel size needed for accurate dosimetry

NMR microscopy of in-vitro trabecular bone samples can easily achieve image resolutions in the range of 50 to 100 µm within reasonable acquisition times (7 to 20 hours). Nevertheless, decreases in voxel dimensions must be accompanied by increases in image acquisition time to counteract loss of signal-to-noise. Consequently, it is instructive to know what voxel dimension is required for accurate radiation dosimetry. Above this dimension, one will expect errors in dosimetry to occur (voxels are too large to model properly the bone-marrow interface). Below this dimension, improvements in dosimetry will not be cost-effective as larger

voxel dimensions should suffice. At the onset, it was realized that the demands of the imaging systems for radiation dosimetry will be less stringent than for applications of biomechanical modeling of the bone trabeculae. In the latter, each trabecula must be accurately represented so as to preserve connectivity between adjacent trabeculae within the skeletal lattice. In the simulation of electrons and beta particles, energy deposition is averaged across the entire structure, and thus slight errors in imaging might not be as important.

In this study, a mathematical model of trabecular bone was constructed in which spheres of marrow were placed within a cubical sample of bone (2, 3). The spaces between the marrow spheres thus represent the bone trabeculae. While the model only approximately describes the true trabecular microstructure, the distribution of sphere radii and their placements within the bone cube were carefully chosen so that chord-length distributions traced across the entire object faithfully represented the bone and marrow chord distributions measured by Whitwell in the cervical vertebra of Reference Man. Electron sources in the marrow spaces were thus modeled in EGS4 and absorbed fractions to bone and marrow were tabulated as a local “gold standard”. Next, the mathematical model was “voxelized” so as to represent an NMR microscopy image of voxels ranging from 16 μm to 1000 μm . For each simulated NMR image of the mathematical bone sample, identical EGS4 electron transport simulations were then performed. The results were then compared to those from the “gold standard” non-voxelized geometry. These comparisons indicated that marrow volume fractions were preserved at image resolutions as low as 300 μm , much greater than current abilities of NMR microscopy (50-100 μm). For self-irradiation of the marrow tissues, no error in dosimetry was noted at resolutions below 300 μm for high-energy emitters, while errors of only 2-5% were seen for low-energy emitters. Errors in the cross-dose to bone were minimal for high-energy emitters, but could approach 25% for very low-energy emitters. The reason for problems in cross-dose at low energies was attributed to an overestimate of the bone-marrow interface by as much as 50% within voxelized images at high resolution. These problems will be addressed in Phase III studies in which polygonal descriptions of the bone-marrow interface will be utilized during electron transport.

3. Studies to determine the precision of the image acquisition, image processing, and transport methodology

In a recent study by Patton et al. (4), a rectangular prism of spongiosa sectioned from the femoral head of the 51-year male was used to quantify the precision of the entire image acquisition, image processing, and radiation transport methodology. Following initial marrow digestion, the sample was repeatedly immersed in Gd-doped water and imaged at 4.7 T using the 3D spin-echo pulse sequence discussed above. Following each of the 5 imaging sessions, regions of interest were selected within the 3D images, coupled to EGS4, and electron sources in the marrow cavities were simulated. Results of the repeated imaging and transport simulations are shown in Figs. 1 and 2 for irradiation targets consisting of the trabecular marrow space (TMS) and the trabecular bone endosteum (TBE), respectively. In Fig. 1, the absorbed fraction to marrow begins at unity and decreases as electron energy is increasingly lost to the surrounding bone trabeculae. In this study, the transport was conducted under the infinite trabecular-region transport geometry and thus convergence values are approached at high energies. Visual inspection of the 2D images from Session 1 indicated that the sample had not been optimally placed within the quadrature coil possibly due to sample movement within the imaging container. Furthermore, this image indicated the presence of air bubbles. No artifacts were noted, however, during a review of the 2D slices from images acquired in Sessions 2-5. The study thus concluded that visual inspection of the images is crucial prior to radiation transport simulations. In comparing the results from Sessions 2-5, an overall experimental precision error of at most 4% is noted at high energies.

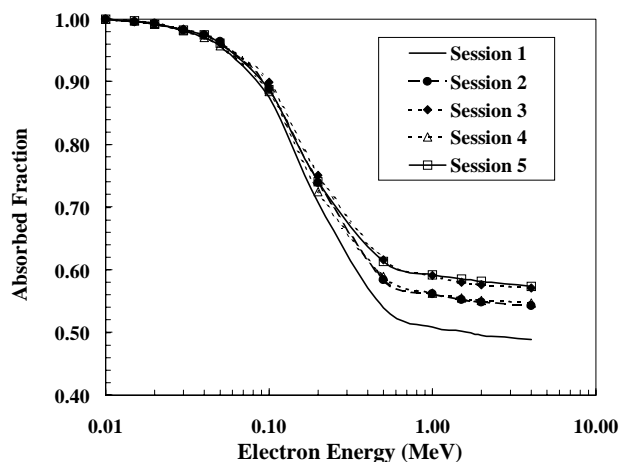


Figure 1. A comparison of absorbed fractions $\phi(\text{TMS} \leftarrow \text{TMS})$ for all five imaging sessions under an infinite medium transport model. The bone prism used for the comparison was sectioned from a femoral head of the 51-year-old male cadaver.

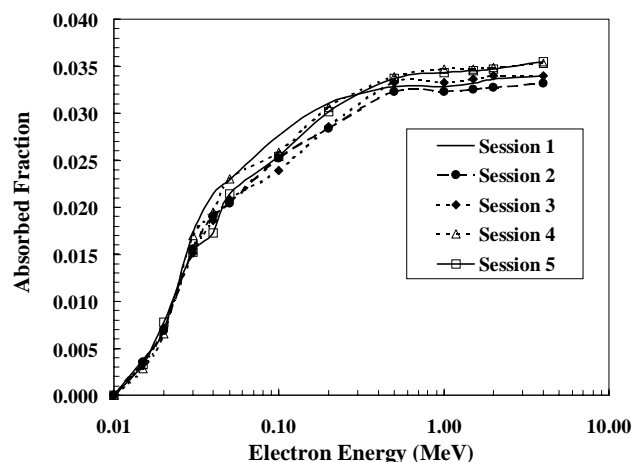


Figure 2. A comparison of absorbed fractions $\phi(\text{TBE} \leftarrow \text{TMS})$ for all five imaging sessions under an infinite medium transport model. The bone prism used for the comparison was sectioned from a femoral head of the 51-year-old male cadaver.

4. Studies of signal source – marrow free versus marrow intact samples

The study by Patton et al. (4) additionally looked at the feasibility of imaging marrow-intact samples of trabecular bone. Fig. 3 shows the results of transport simulations of an electron source in the marrow cavity of the femoral head of a 71-year male subject. The femoral head was excised during total hip arthroplasty, was sectioned immediately following surgery, and was imaged at 4.7 T within four hours. Latter, the sample was subjected to marrow digestion and re-imaged after immersing in Gd-doped water. Targets are the trabecular marrow space (TMS), trabecular bone volume (TBV), and the trabecular bone endosteum (TBE). A maximum variation of only 4% (within our experimental precision error) is seen at the most extreme energy between the two signal sources. The study was also repeated using marrow-intact trabecular bone samples taken from the right femoral head of the 51-year male cadaver. As shown in Fig. 4, the reproducibility of the imaging/transport method is even better for this particular bone sample. The study concludes that either marrow-intact or marrow-free samples may be used for NMR microscopy and radiation transport studies.

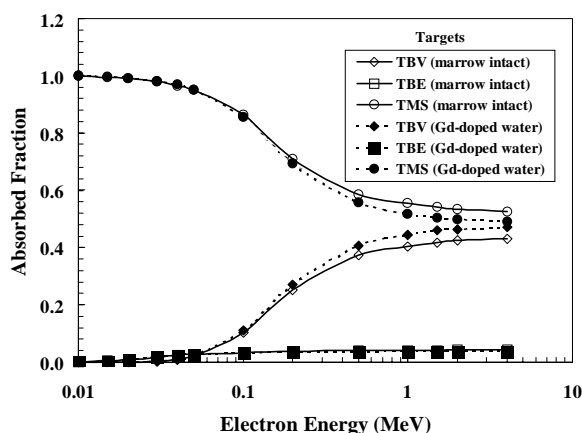


Fig. 3. Comparisons between absorbed fractions for a TMS electron source calculated using 3D NMR microscopy of a bone cube with either intact marrow within the marrow cavities, or Gd-doped water filling the marrow cavities following marrow digestion. The bone prism used was physically sectioned from the right femur head obtained from a 71-year-old male undergoing total hip arthroplasty.

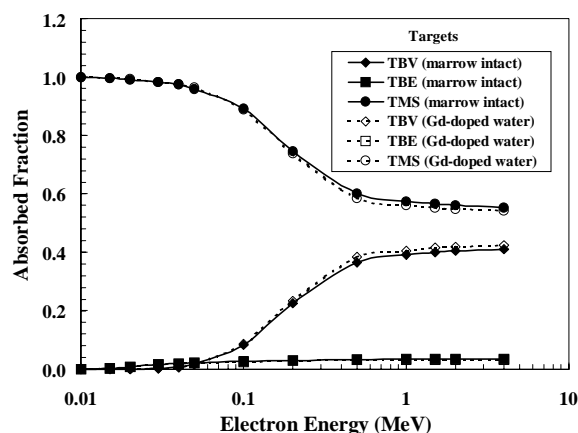


Fig. 4. Comparisons between absorbed fractions for a TMS electron source calculated using 3D NMR microscopy of a bone prism with either intact marrow within the marrow cavities, or Gd-doped water filling the marrow cavities following marrow digestion. The bone cube used was physically sectioned from the right femoral head harvested from a 51-year-old male cadaver.

5. Introduction of marrow cellularity into the 3D radiation transport models

Both the Bouchet et al. (5) and the Eckerman and Stabin (6) chord-based models are forced to make rather dramatic assumptions regarding the impact of marrow cellularity on the pattern of energy deposition by electrons as they traverse marrow cavities. With the advent of 3D transport models based on microimaging of the trabecular architecture, explicit differentiation of the marrow tissues in their active and inactive components is now feasible (7). Shown in Figs. 5 and 6 are 2D slices from segmented and filtered 3D images of trabecular bone in which three-voxel groupings of inactive marrow are introduced representing clusters of adipocytes. The positioning of the clusters are based upon visual observations of biopsy slides of normal bone marrow in which cluster size distributions and fractional bone perimeter coverage were assessed and recreated within the 3D digital image (8). True trabecular active marrow (TAM) sources of electrons were thus simulated at marrow cellularities ranging from 10% to 100%, the latter corresponding to a trabecular marrow space (TMS) source of electrons. Fig. 7 displays absorbed fractions using the macrostructural transport model for the self-irradiation of the active marrow within the femoral head of the 51-year male. Five values of marrow cellularity are assumed: 10, 30, 50, 80, and 100%.

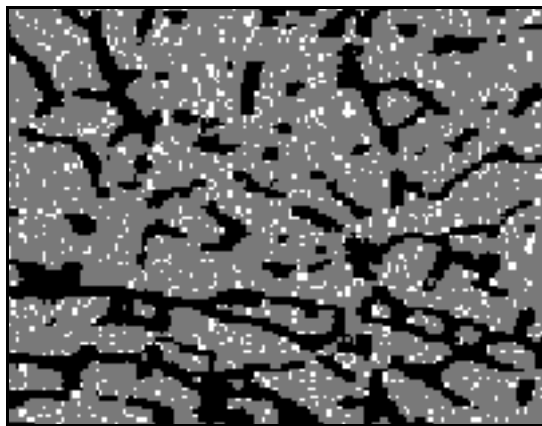


Fig. 5. A 2D region of interest selected from a 3D NMR image of a trabecular bone sample sectioned from the femoral head of a 51-year male. Black voxels represent bone trabeculae, white voxels represent active marrow (10% cellular), and gray voxels represent inactive marrow (adipocytes clusters).



Fig. 6. An identical slice through the 3D as shown in Fig. 5, except that the marrow cellularity is set 80% (20% fat fraction).

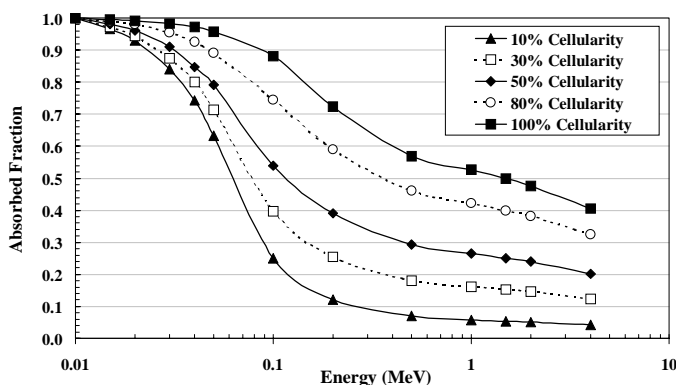


Fig. 7. Electron absorbed fractions $\phi(\text{TMS} \leftarrow \text{TMS})$ calculated for marrow cellularities of 10%, 30%, 50%, 80%, and 100% using the macrostructural transport model for the femoral head of the 51-year-old male. The values shown are the average absorbed fractions of two separate bone samples sectioned from the femoral head (<4% variation at high energies).

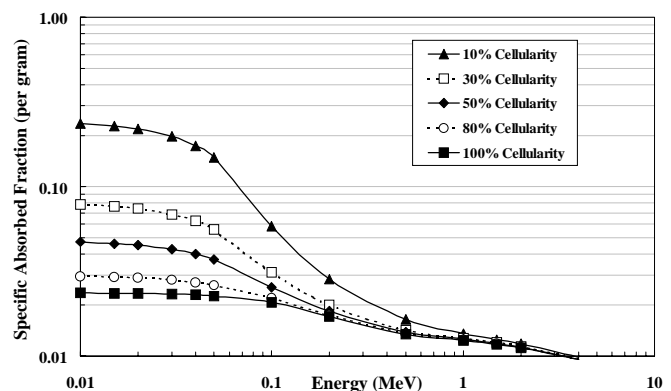


Fig. 8. Values of specific absorbed fraction based on the identical data given in Fig. 7. The specific absorbed fraction can be interpreted as the absorbed dose per decay for monoenergetic electron sources. Weighting the specific absorbed fraction across the energy spectrum of a beta-emitting radionuclide will thus yield the radionuclide S value.

The self-absorbed fractions for electron sources in the active marrow of the male femoral head are shown to separate from one another at high energies in direct proportion to the reduction in active marrow target mass. Consequently, it is instructive to normalize the absorbed fractions at each value of marrow cellularity by the corresponding TAM target mass. Values of specific absorbed fraction, $\Phi(\text{TAM} \leftarrow \text{TAM})$, are thus shown in Fig. 8. For high-energy electron emitters (energies exceeding several hundred keV), the mean dose per decay to active marrow is shown to be independent of the marrow cellularity. At high energies, the electrons more or less uniformly traverse the marrow cavities resulting in a uniform distribution of imparted energy to all marrow tissues. At high energies, both the active and inactive marrow components experience the same absorbed dose independent of their respective volume fractions within the marrow space. As one considers lower and lower energy emissions within the active marrow, however, the spatial separation of the active and inactive marrow tissues becomes increasingly important, particularly at low cellularities (high fat fractions). Fig. 8 shows that the mean dose per decay to active marrow for 10 keV electrons is a factor of 3 higher than in marrow of 30% cellularity. For marrow at 50% cellularity, the dose per decay delivered by 10 keV electrons is a factor of 0.6 lower than at 30% cellularity. For low-energy emitters in the energy range of 10 to 100 keV, the specific absorbed fractions, and thus the radionuclide S values, vary considerably with marrow cellularity, a factor that is not considered in the current Reference Man skeletal model.

Fig. 9 displays the absorbed fraction profiles for a TAM source and target in the femoral head of the male using two published methodologies and compares those results to values obtained via direct radiation transport. In these comparisons, the radiation transport results utilize a “reference” cellularity of 0.25 for the femoral head (solid line – no data points). Two additional values (dashed lines) are shown for 10% cellularity (lower than average) and 40% cellularity (higher than average). Self-absorbed fractions for the TMS are calculated in this work using an infinite trabecular region transport model as representative of the Bouchet et al. model. Next, this curve is then uniformly scaled by a value of 0.25 at all energies to produce absorbed fractions representative of the Eckerman and Stabin model.

Fig. 9 shows that the method used by Eckerman and Stabin greatly underestimates the absorbed fraction to active marrow for electron energies below 200 keV. In fact at 10 keV, their method underestimates the TAM absorbed fraction by as much as 75% as defined in their scaling approach. At electron energies above 200 keV, however, their method produces results that differ by less than 5% from the absorbed fractions calculated in this work, provided that the assumed reference cellularity of 25% is appropriate to the patient in question. As shown by the dashed lines, the absorbed fraction can vary over a factor of 3.5 at high energies for corresponding cellularity variations ranging from 10 to 40%. At 4 MeV, their method begins to overestimate the TAM self-absorbed fractions by a factor of 1.3 in that their model does not allow for electron energy escape to the surrounding cortical bone (macrostructural versus infinite-trabecular-region transport). The method of Bouchet et al. is consistent with the absorbed fractions calculated by direct transport at all marrow cellularities only at extremely low electron energies. At 20 keV, this method overestimates the absorbed fraction at reference cellularity by a factor of 1.05, and by as much as a factor of 5.3 at 4 MeV. In the energy range of 20 keV to 200 keV, neither method accurately predicts the fraction of electron energy absorbed within the active tissues of the marrow cavities.

In both the methods of Bouchet et al. and Eckerman and Stabin, absorbed fractions are divided by the active marrow mass in Reference Man ($0.25 \times$ total marrow mass) to obtain corresponding values of $\Phi(\text{TAM} \leftarrow \text{TAM})$. Consequently, discrepancies in $\phi(\text{TAM} \leftarrow \text{TAM})$ shown in Fig. 9 are reflected in corresponding values of $\Phi(\text{TAM} \leftarrow \text{TAM})$ as shown in Fig. 10. The method of Eckerman and Stabin preserves values of mean dose to active marrow per electron emission with changes in marrow cellularity for high-energy electron sources. As the source energy decreases, however, the model of Bouchet et al. is shown to provide accurate dosimetry at energies of 30 keV and less, provided that the assumed reference cellularity is justified for that particular patient. If the patient’s marrow cellularity is lower than normal (10% in the extreme), the dose per low-energy electron emission is shown to be a factor of 2.5 times higher than predicted by Bouchet et al. and a factor of 10 times higher than that predicted by the Eckerman and Stabin model.

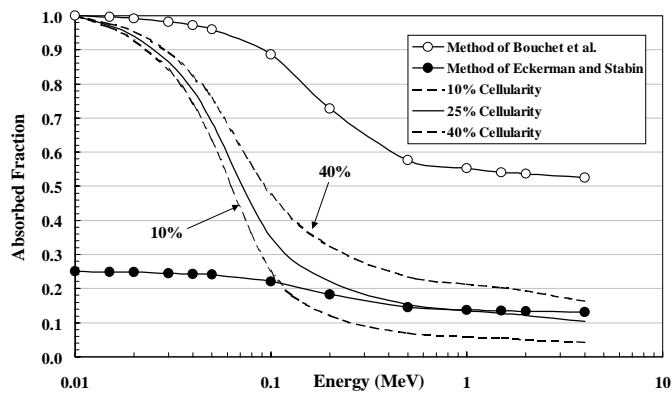


Fig. 9. Electron absorbed fractions for self-irradiation of the trabecular active marrow (TAM) within the femoral head of the 51-year male. Three dosimetry methodologies are compared. The TAM self-absorbed fractions reported in this work are directly calculated using the macrostructural transport model of the EGS4 transport code (solid line – no points). Dashed lines indicate potential variations with changes in individual marrow.

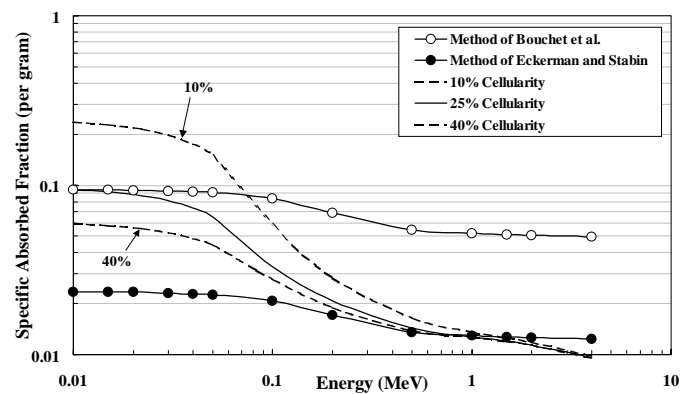


Fig. 10. Electron specific absorbed fractions for self-irradiation of the trabecular active marrow (TAM) within the femoral head of the 51-year male. These values are obtained by dividing each curve in Fig. 9 by the corresponding mass of active marrow. Dashed lines indicate potential variations in the specific absorbed fraction with changes in individual marrow cellularity either lower (10%) or higher (40%) than that of Reference Man (40%).

6. Considerations of energy loss to cortical bone

One limitation of the current Reference Man skeletal models, as published by either Eckerman and Stabin or by Bouchet et al., is that electrons are followed within an infinite expanse of trabecular skeleton. In our NMR microscopy studies, we have implemented macrostructural models of the thoracic vertebra of a 52-year male (1). Recently, these models were extended to include the femoral head and humeral epiphyses of a 51-year male, an 82-year female, and a 86-year female (9). In each model the physical size of the spongiosa and the thickness of the cortical bone cortex were assessed via CT analysis prior to spongiosa sectioning. In these later models, electrons are permitted to leave the spongiosa of the skeletal site and deposit energy within the cortical bone cortex, or even escape the bone site entirely. Figs. 11 and 12, we display absorbed fraction data from both the infinite trabecular transport model (solid lines) and the macrostructural transport model (dashed lines) in the femoral head and in the humeral epiphysis, respectively, of the 86-year female. In Fig. 11 the total marrow space is both the source and target, while in Fig. 12, the marrow is irradiated by electrons emitted from within the bone trabeculae. In Fig. 11, two curves are shown for each model: one from each of two sectioned bone prisms (S1 and S2) from the subject's femoral head. The smaller size of the humeral epiphysis permitted the sectioning of only one bone sample. The variation between samples in Fig. 11 indicates that potential regional variations in trabecular microstructure are within the precision error of the imaging/transport method. Greater variations are seen, however, between the two bone prisms taken from the 82-year female, thus acknowledging intra-skeletal site variations in trabecular microstructure and must be taken into account when the bone sites are sectioned.

In the femoral head of this individual, it is noted that the infinite region transport geometry potentially overestimates the absorbed fraction of energy to marrow at electron energies as low as 1 MeV. In the smaller humeral epiphysis of the same individual, deviations in energy deposition between the two transport geometries are noted at even lower energies (several hundreds of keV). In Patton et al. (9), we estimated ratios of mean absorbed fractions under both transport methodologies for the radionuclides ^{32}P and ^{90}Y by weighting the absorbed fraction data over their beta energy spectra. These ratios indicate that corrections to existing radionuclide S values for ^{32}P can vary by as much as 5.4% for the male, 6.4% for the 82-year female, and 7.9% for the 86-year female. For the higher-energy beta spectrum of ^{90}Y , these same corrections can be as high as 8%, 10.2%, and 11.3%, respectively. We conclude, therefore, that macrostructural models of skeletal dosimetry are needed, particularly for high-energy electron sources and skeletal sites of small spongiosa dimensions.

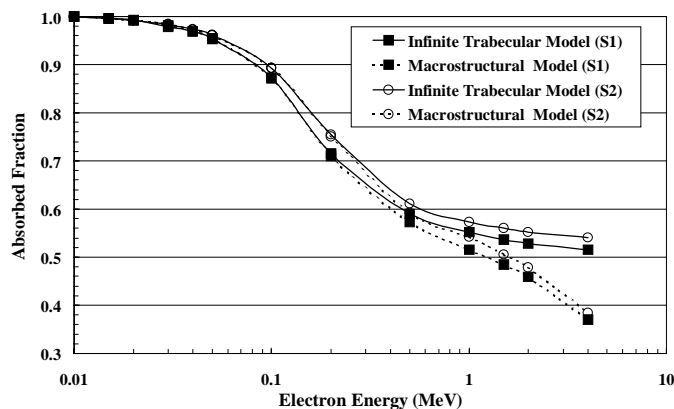


Fig. 11. Comparison of absorbed fractions $\phi(\text{TMS} \leftarrow \text{TMS})$ calculated using the infinite trabecular region transport and the macrostructural transport model, respectively, for the femoral head of an 86-year-old female cadaver.

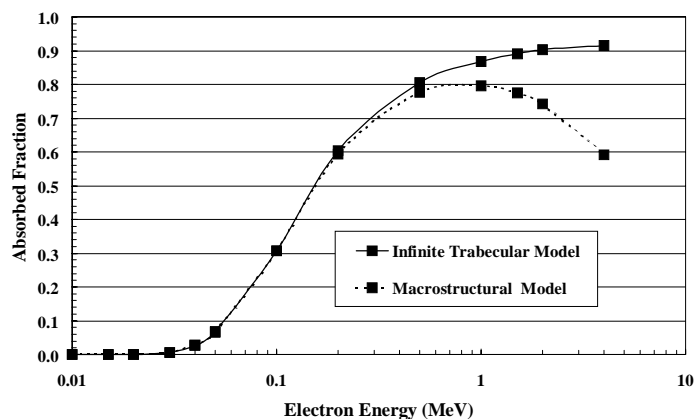


Fig. 12. Comparison of absorbed fractions $\phi(\text{TMS} \leftarrow \text{TBV})$ calculated using the infinite trabecular region transport and the macrostructural transport model, respectively, for the proximal humeral epiphysis of an 86-year-old female cadaver.

7. Studies of individual variability in skeletal dosimetry – femoral head and humeral epiphysis

In Patton et al. (9), we look further at individual variability in the marrow dosimetry of the femoral heads and humeral epiphyses of the 51-year male, 82-year female, and 86-year female. In order to highlight only differences in both the trabecular microstructure and overall physical dimensions of the skeletal sites, we have purposely not made a distinction between active and inactive marrow in the transport models of this study. The conclusions drawn from the discussion in Section 5, however, are nevertheless still valid for all subjects. Data on electron absorbed fractions for self-irradiation of the total marrow in these skeletal sites are shown in Fig. 13 below. Here we see dramatic differences in the pattern of absorbed fractions in the humeri than in the femoral heads for all individuals, but particularly apparent in the females. The higher values of absorbed fraction in the humeri are directly attributable to the higher marrow volume fraction of that skeletal site. As shown in Table 1 below, the marrow composes $\sim 75\%$ of the spongiosa volume in the femoral head of the 82-year female, while $\sim 96\%$ of the spongiosa volume is comprised of marrow within her humeral epiphysis. The data are consistent with our understanding of the different biomechanical loads on the femoral and humeral trabeculae, with less loads applied to the latter and thus less bone formation is required during skeletal remodeling. Clearly the different trabecular microstructure has implications on the regional marrow dosimetry of that skeletal site. Shown for comparison is the absorbed fraction energy profile of Reference Man as assessed through the transport model of Bouchet et al. (10). In the original work by Spiers' student J.R. Whitwell, microstructural data were not acquired in the humerus; consequently, the Reference Man model implicitly assumes that the humeral dosimetry is 80% that of the femoral head and 20% that of the femoral neck, where the latter two sites were measured. Fig. 13 clearly shows that this assumption is poor, especially for the two female individuals.

As the physical size and bone volume fractions of the skeletal sites change among the three individuals in the study, the total mass of marrow target tissue changes accordingly as shown in Table 1. Consequently, it is instructive to normalize the absorbed fractions shown in Fig. 13 by the corresponding TMS target mass. As defined in the MIRD schema, the resulting values of specific absorbed fraction $\Phi(\text{TMS} \leftarrow \text{TMS})$ are directly proportional to the mean dose to total marrow per particle emission. A spectral weighting of these values gives the radionuclide S value.

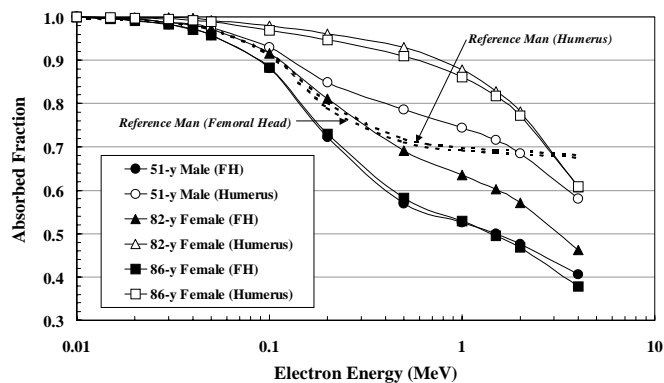


Fig. 13. Monoenergetic electron absorbed fractions $\phi(\text{TMS} \leftarrow \text{TMS})$ for the self-irradiation of the total marrow within the femoral head (solid symbols) and humeral epiphysis (open symbols) of the 51-year male, 82-year female, and 86-year female. All energy profiles are made under the macrostructural transport model. The femoral head data shown here have been averaged from those given by the two bone prisms sectioned from that skeletal site.

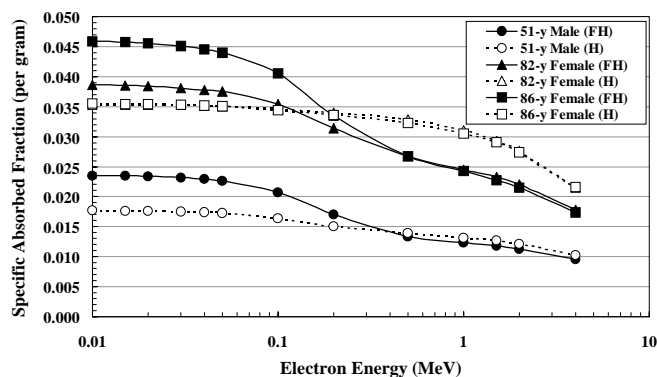


Fig. 14. Specific absorbed fractions $\Phi(\text{TMS} \leftarrow \text{TMS})$ for the self-irradiation of the total marrow within the femoral head and humeral epiphysis of the 51-year male, 82-year female, and 86-year female. The data shown are based on the absorbed fraction data shown in Fig. 13 and the mass estimates given in Table 1.

Table 1. Estimates of spongiosa total volume, volumes of marrow, and masses of marrow within the femoral heads and humeral epiphyses of each of the three subjects in the study. Volumetric fractions of spongiosa for the trabecular marrow space (TMS) are determined via the segmented NMR images. Where more than one bone prism samples was obtained, the volume fractions given below are averaged across both samples.

	51-year Male		82-year Female		86-year Female	
	Femoral Head	Humeral Epiphysis	Femoral Head	Humeral Epiphysis	Femoral Head	Humeral Epiphysis
Volume of Spongiosa (cm ³)	65.4	65.4	33.5	28.7	33.5	28.7
TMS Volume Fraction	0.63	0.84	0.75	0.96	0.63	0.95
TMS Volume (cm ³)	41.2	55.0	25.1	27.5	21.1	27.4
TMS Mass (g)	42.5	56.6	25.9	28.3	21.8	28.2

Fig. 14 thus displays values of the specific absorbed fraction for the self-irradiation of the total marrow in each of the two skeletal sites and for each of the three individuals. At energies of ~ 500 keV and higher, a convergence of the specific absorbed fractions is seen for three pairs of skeletal sites each with identical volumes. At these higher energies, electrons lose energy in bone tissue almost as efficiently as in marrow (stopping power ratios of about 1.1), and thus high-energy electrons deposit their energy nearly uniformly across the spongiosa. The dose to total marrow for high-energy electrons is thus primarily a function of the physical size of the bone site and not its total marrow mass. This is a key feature when scaling dosimetry data from a reference individual to a given patient as the skeletal volume should be the basis of scaling. As the energy of the source electrons decrease, these curves separate according to their differences in marrow volume fraction (as potentially assessed via vBMD measurements). For example, the spongiosa interior to the femoral heads of the two females were noted to be of equal volume, yet the mass of marrow is higher in the 82-year female than in the 86-year female (25.9 g versus 21.8 g). The corresponding dose to marrow per electron emission is thus lower in the 82-year femoral head (see Fig. 14). Scaling of dosimetry data between individuals for low-energy electron sources should thus be made on the product of the spongiosa volume (as for high-energy emitters) and the marrow volume fraction. These concepts are further developed below.

8. Methods of scaling Reference Man data for determining patient-specific radionuclide S values

The data shown in Fig. 14 has lead us to consider making similar comparisons to Reference Man, and to explore both existing and potentially new means of scaling reference skeletal data to improve the patient specificity of radionuclide S values (11). To make this comparison, we first had to determine the equivalent total marrow masses in the femoral head and humeral epiphyses of Reference Man. Using data from ICRP Publication 70 and the analysis by Bouchet et al., we estimate that he has 31.4 g of total marrow in his right (or left) femoral head and 33.6 g of total marrow in his right (or left) humeral epiphysis. Details are given in Appendix E, yet these essentially equivalent masses are consistent with the observation of equivalent volumes in these skeletal sites within our 51-year male. The fact that we have different masses in our 51-year male is due to our knowledge of the marrow volume fraction in our subject; no equivalent microstructural information is available in Reference Man to discern a difference in marrow mass for equal skeletal volume.

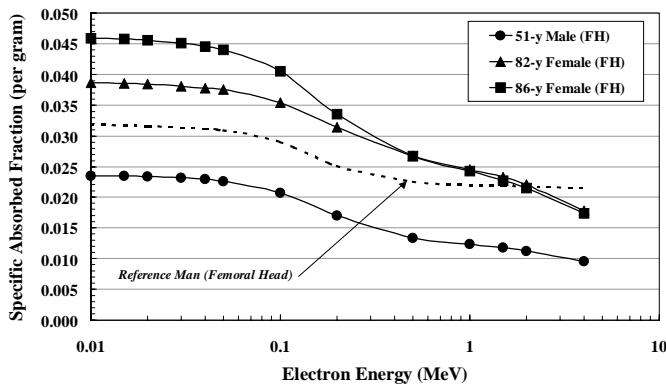


Fig. 15. Specific absorbed fractions $\Phi(\text{TMS} \leftarrow \text{TMS})$ for the self-irradiation of the total marrow within the femoral head of the 51-year male, 82-year female, and 86-year female.

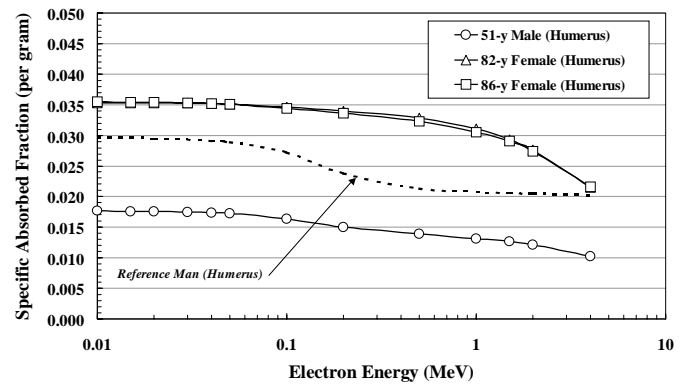


Fig. 16. Specific absorbed fractions $\Phi(\text{TMS} \leftarrow \text{TMS})$ for the self-irradiation of the total marrow within the humeral epiphysis of the 51-year male, 82-year female, and 86-year female.

Using these mass estimates, we plot in Figs. 15 and 16 values of $\Phi(\text{TMS} \leftarrow \text{TMS})$ within the femoral head and humeral epiphysis, respectively, for each of the three subjects as well as for Reference Man. In Fig. 15, we note that the slope of the curves are similar at low energies, but differ at high energies in that the Reference Man model does not account for energy escape to cortical bone. In Fig. 16, we see a mismatch of slopes between Reference Man and the humeral data for the three subjects, especially for the female subjects. Here, the differential trabecular microstructure of the humerus is not properly accounted for in Reference Man.

As shown in Figs. 17 and 18, we next explore various morphometric scaling parameters in our attempts to shift upward or downward values of $\Phi(\text{TMS} \leftarrow \text{TMS})$ for Reference Man to match the corresponding data of the 82-year female and 86-year female, respectively (see Appendix E). Scaling parameters used include total height, total mass, lean body mass (via biometric expressions of height and mass), and body mass index. When scaling by lean body mass, it was not clear to us whether physicians/dosimetrists make a similar adjustment to the total body mass of Reference Man (70 kg). Consequently, we additionally scale by the total-to-lean body mass ratio (70 kg/LBM of patient). In attempting to match the femoral head data of the 82-year female, we find that total body mass and BMI scale Reference Man in the wrong direction. At low energies, total-to-lean mass scaling is best. At higher energies, no scaling method is optimal as the shapes of the specific absorbed fractions are not equivalent at those energies. For the 86-year female, scaling by BMI or lean body mass is best at low energies, with height scaling or even no scaling serving as the better choice at high energies. We note in Bolch et al. (11) that “while some parameters give very good agreement for a particular person, a particular energy range, and a particular skeletal site, no consistent scaling parameter emerges when one considers the full range of parameter combinations. The situation, however, is not totally surprising as Reference Man is an amalgamation of biometric and morphometric data, and, differences between the trabecular microstructural of these two skeletal sites are not accommodated in that model.”

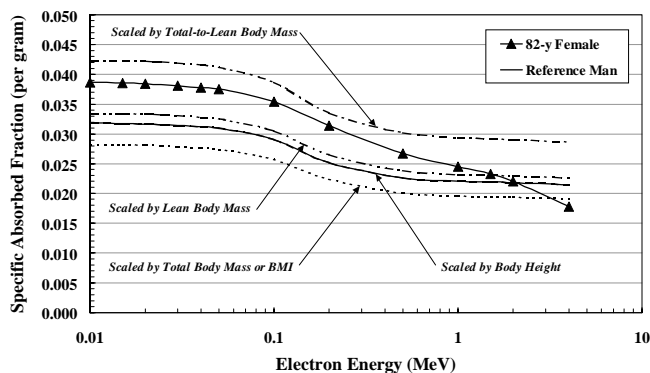


Fig. 17. Results of various approaches to proportional scaling of Reference Man values of $\Phi(\text{TMS} \leftarrow \text{TMS})$ within the femoral head needed to match the data for the 82-year female.

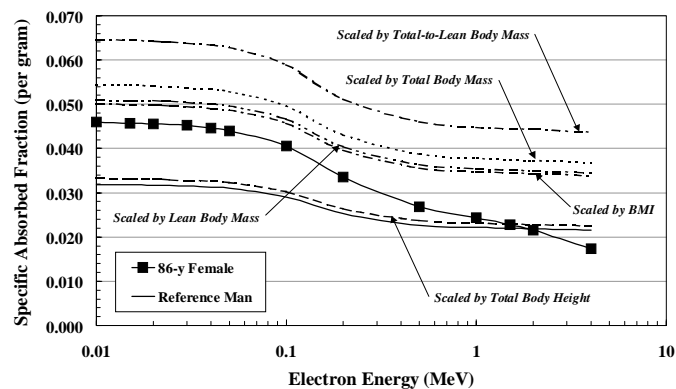


Fig. 18. Results of various approaches to proportional scaling of Reference Man values of $\Phi(\text{TMS} \leftarrow \text{TMS})$ within the femoral head needed to match the data for the 86-year female.

These comparisons suggested to us that improved matching of the female data can be accomplished by scaling our data of the 51-year male. In effect, he becomes the reference skeletal model. Thus, attempts to match the femoral head data of the two females was made accordingly as shown in Figs. 19 and 20. In both cases, scaling by lean body mass appears suitable for both female subjects. The match is better for the 82-year female at lower energies than at higher energies. For the 86-year female scaling by body mass index provides a virtually perfect scaling at all energies. While not totally conclusive, these attempts appear to show a more consistent in matching the female dosimetry data than by use of Reference Man data.

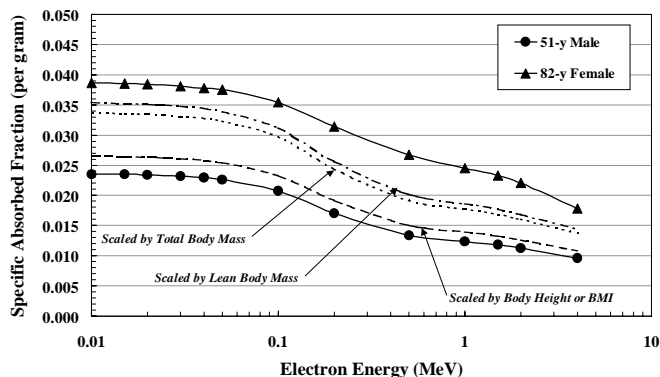


Fig. 19. Results of various approaches to proportional scaling of values of $\Phi(\text{TMS} \leftarrow \text{TMS})$ within the femoral head of the 51-year male needed to match the data for the 82-year female.

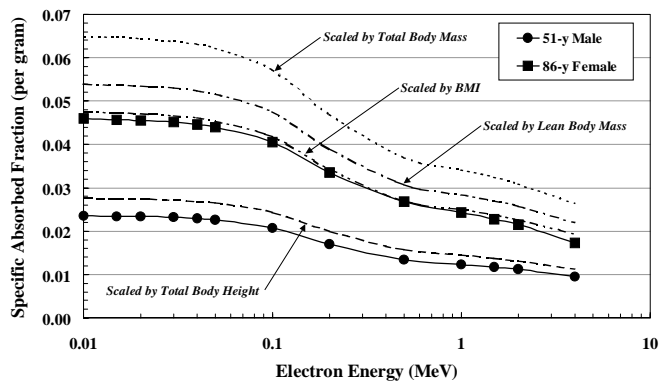


Fig. 20. Results of various approaches to proportional scaling of values of $\Phi(\text{TMS} \leftarrow \text{TMS})$ within the femoral head of the 51-year male needed to match the data for the 86-year female.

The scaling results shown above for Reference Man (Figs. 17 and 18) and for the 51-year male (Figs. 19 and 20) are generally somewhat arbitrary attempts at re-adjusting the absorbed fractions and/or target masses used in the definition of $\Phi(\text{TMS} \leftarrow \text{TMS})$. The previous analysis of the macrostructural transport data in Section 7, however, provides more specific methods for scaling skeletal dosimetry data from one individual to another. For example, in Fig. 21 we attempt once more to scale values of $\Phi(\text{TMS} \leftarrow \text{TMS})$ for the 51-year male to those calculated for the 82-year female. Two scaling methods are used. We first scale by the ratio of spongiosa volumes measured in these two individuals. Here we see the agreement at energies 300 keV and higher. Next, we scale by ratios of (spongiosa volume) \times (marrow volume fraction) or (total marrow volume). For this latter scaling, good agreement is seen at energies below ~ 40 keV. In the transition energy range of 40 keV to 300 keV, both the physical size of the skeletal site and its internal microstructure (marrow volume fraction) play roles in the absorbed dose to marrow per particle emission. Consequently, a weighted average of the two different scaling parameters must be applied. When applied together, we achieve a nearly exact scaling across

all energies, and thus S values for all radionuclides may be appropriately assigned to the patient. The key to this proposed scaling methodology, however, is that skeletal volumes and marrow volume fractions must be known in both the patient and in the reference skeletal model. Clearly, the current Reference Man model is insufficient, and new reference skeletal models must be developed.

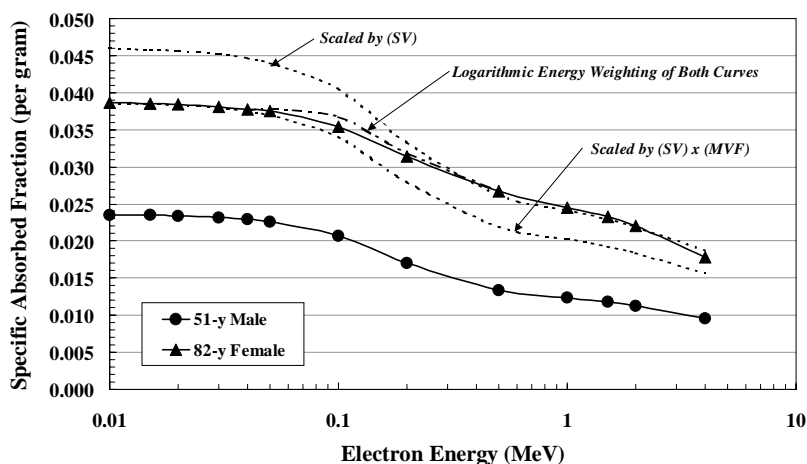


Fig. 21. Demonstration of optimal matching of values of $\Phi(\text{TMS} \leftarrow \text{TMS})$ in the femoral heads of the 51-year male and 82-year female whereby scaling by spongiosa volume is performed at high electron energies and total marrow volume scaling is accomplished at low electron energies.

The agreement shown in Fig. 21 is not surprising as detailed information on spongiosa volumes and marrow volume fractions are known in both the reference individual (51-year male) and the “patient” (82-year female). If this data is only available in the reference individual, the question then becomes how can these scaling parameters be estimated in a real patient? Two scenarios are conceived. First, let us assume that the patient is undergoing radionuclide therapy in which accurate and localized marrow dosimetry is desired (e.g., lumbar vertebrae). A regional high-resolution CT exam will most certainly provide the imaging data needed to assess spongiosa volumes and volumetric bone mineral density (vBMD). “Exact” scaling of radionuclide S values is thus possible as indicated in Fig. 21 for this group of patients. The second scenario will be such that a localized CT exam will either not be available or would not be justified. In this case, scaling by spongiosa volume needed for high-energy beta emitters must be made using more easily measurable morphometric parameters (body height, body mass index, etc.). We have performed a very preliminary literature search to see what parameters might scale with skeletal volume (not mass); no specific information has yet emerged from this effort. For low-energy emitters, one must estimate the marrow volume fraction in skeletal sites of interest. Here, we propose that a DEXA measurement of areal bone mineral density (aBMD) might suffice if this same information were available in the reference individual. If a new reference male and female skeletal model were developed, we contend that CT exams of therapy patients will give sufficient information to obtain highly patient-specific radionuclide S values for marrow dosimetry. With further research on skeletal volume scaling, and the use of DEXA measurements of BMD, routine scaling of reference skeletal S values can be made for all groups of patients. The first step, however, is to redefine the reference skeletal models with imaging and dosimetry information of sufficient detail to implement the scaling methodology.

9. Absorbed Fractions for Alpha-Particles and Neutron Recoils

A computer code was developed to calculate heavy charged particle (HCP) transport in trabecular bone. This code calculates the absorbed fraction in each of the trabecular region constituents: trabecular bone, active (red) marrow, and inactive (yellow) marrow. The transport model uses the Continuous Slowing Down Approximation (CSDA) range. Data for CSDA ranges was obtained from the National Institute of Standards and Technology (NIST) ASTAR and PSTAR databases. The atomic composition and density data for the trabecular constituents was taken from International Commission on Radiological Units and Measurements (ICRU) Publication 49. From these data sets energy-range relationships were developed for several HCPs

including: alpha particles, protons, and recoil carbon, nitrogen and oxygen nuclei. Figure 22 provides a plot of the proton range relationship.

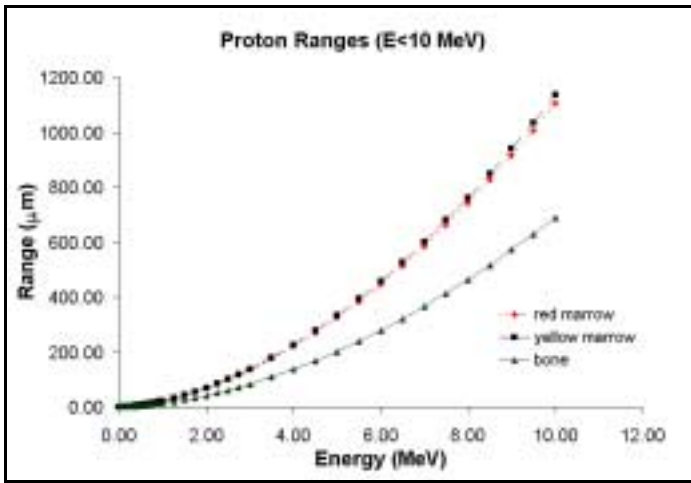


Fig. 22. Proton ranges in Trabecular bone tissues for protons with energy less than 10 MeV. Range data from NIST PSTAR database.

The range relationship for alpha particles was obtained directly from the NIST ASTAR database similar to the protons. Recoil nuclei range relationships were obtained using scaling laws based upon the Beta value of protons and the equivalent recoil nuclei. The following equations demonstrate the relationships used to obtain these range relationships.

$$R(\beta_2) = \frac{(m_o c^2)_2}{(m_o c^2)_1} \frac{z_1^2}{z_2^2} R(\beta_1) \quad (\text{Eq. 1})$$

$$\frac{\beta_2}{\beta_1} = 1 = \frac{(m_o c^2)_1}{(m_o c^2)_2} \frac{T_2}{T_1} \quad (\text{Eq. 2})$$

From these relationships similar energy-range relationships were obtained for the recoil nuclei with the PSTAR proton data being the standard (particle 1 in the equations). A curve fit was then obtained for each energy-range relationship and used in the HCP transport model.

The transport model was then used to calculate absorbed fractions for alpha particles, protons, and recoil carbon, nitrogen and oxygen nuclei. Alpha particles and protons were calculated for energy ranges from 1.0-MeV to 10.0-MeV. The maximum energy for protons was chosen as 10.0 MeV since this is the maximum energy which may be transferred to a proton by a n,p collision. The same energy range was chosen for alpha particles so that a comparison of alpha particle and proton absorbed fractions could be made. A similar strategy was used in determining the energy range for the carbon, nitrogen and oxygen recoil nuclei. Equation 3 was used to determine the maximum energy transferred to each recoil nuclei.

$$\frac{E_{tr}}{E_n} = 2 \frac{M m_n}{(M + m_n)^2} \quad (\text{Eq. 3})$$

E_{tr} is the energy transferred to the particle M from the collision with a neutron m_n and initial energy E. Table 2 illustrates the resulting energy transfer ratios and the maximum energy for each recoil nuclei.

Table 2. Maximum energy transferred from 20 MeV neutrons to a recoil nucleus.

Recoil Nuclei	Maximum Energy Transfer Ratio	Maximum Energy Transferred (MeV)
proton	0.5	10
Carbon	0.142	2.84
Nitrogen	0.124	2.48
Oxygen	0.083	1.66

Absorbed fractions were then calculated for each recoil nucleus type with a maximum energy as related in Table 2. Initial studies have been done with NMR images of a 52-year old male humeral epiphysis and an 82-year old female femur head. Absorbed fractions were obtained for alpha particle transport in the male humeral epiphysis. Trabecular active marrow (TAM) and trabecular bone volume (TBV) sources were studied with trabecular active marrow being the target. The same source-to-target relationships were also studied using the female femur head, using proton and recoil nuclei. Each study also incorporated various cellularities into each image using either geometric or random placement.

Figure 23 illustrates alpha particle absorbed fractions for a TAM source with a TAM target, while Figure 24 presents a TBV source. In Figure 23, the absorbed fraction is seen to decrease with decreasing cellularity and increasing energy. The ICRP 30 value for alpha particle absorption in TAM from TAM source is 1.0. Our data demonstrates that the ICRP 30 assumption significantly overestimates the absorbed fraction as cellularity decreases. This effect becomes increasingly significant as alpha particle energy increases. Even at 100% cellularity the ICRP 30 value over estimates the absorbed fraction. The TBV source also shows deviation from the assumed 5% absorbed fraction value from ICRP 30. At lower energies the value overestimates the actual absorbed fraction to the TAM, while at higher energies it underestimates the absorbed fraction. For 100% cellularity it overestimates the value by as much as 18%. Absorbed fractions are also seen to vary significantly depending on the cellularity, for which they increase with increasing cellularity. For alpha particles it has been shown that the current approach given by ICRP 30 and used in other bone dosimetry methods is incorrect. Changes in cellularity result in significant differences in absorbed fraction for both TAM and TBV sources.

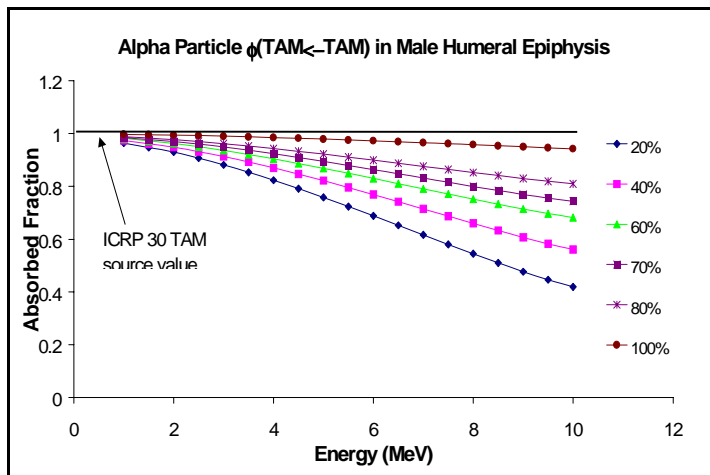


Fig. 23. Absorbed fraction to TAM in male humeral epiphysis for alpha particles from a TAM source with varying cellularity. The absorbed fractions are compared with the ICRP 30 assumption of a 1.0 absorbed fraction for alpha particles with a TAM source.

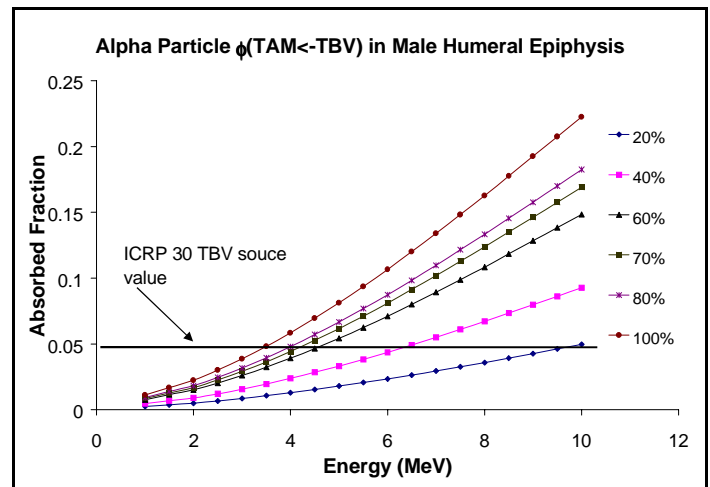


Fig. 24. Absorbed fraction to TAM in male humeral epiphysis for alpha particles from a TBV source with varying cellularity. The absorbed fractions are compared with the ICRP 30 assumption of a 0.05 absorbed fraction for alpha particles from a TBV source.

Figures 25 and 26 illustrate proton absorbed fractions in TAM from TAM and TBV sources respectively. A similar response is seen for protons as for alpha particles. For a TAM source irradiating a TAM target the absorbed fraction decreases with increasing energy and decreasing cellularity. This relationship is even more significant for protons than for alpha particles. TBV sources of protons are also similar to the TBV alpha particle sources. Each demonstrates that as cellularity and energy increase the absorbed fraction to the TAM also increases. This demonstrates that the KERMA approximation, which is generally used in bone dosimetry, does not relate the actual physics of proton transport in the trabecular bone. Recoil nuclei from neutron interactions with carbon, nitrogen and oxygen on the other hand do follow the KERMA approximation in trabecular bone as seen in Figure 27. The absorbed fraction for each recoil nucleus is approximately 0.99. Each relationship shows linearity or near linearity in the absorbed fraction curves. Also if the curves are

extrapolated to lower energies their curves each approach unity for the absorbed fraction. This demonstrates that even for the highest possible energy recoils the KERMA approximation is valid and does relate the physical transport of recoil nuclei in trabecular bone. Therefore only protons become significant when evaluating the KERMA approximation in the trabecular regions of the skeleton.

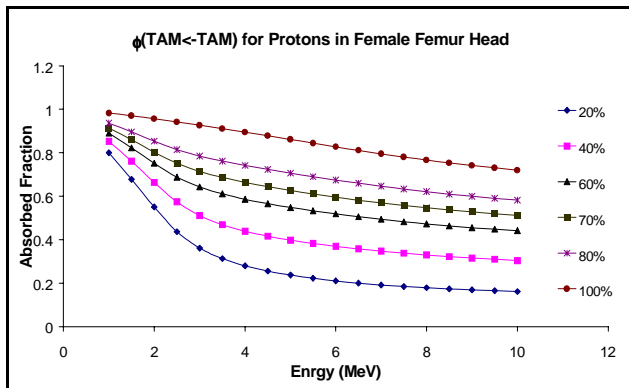


Fig. 25. Absorbed fraction to TAM in male humeral epiphysis for protons from a TAM source with varying cellularity.

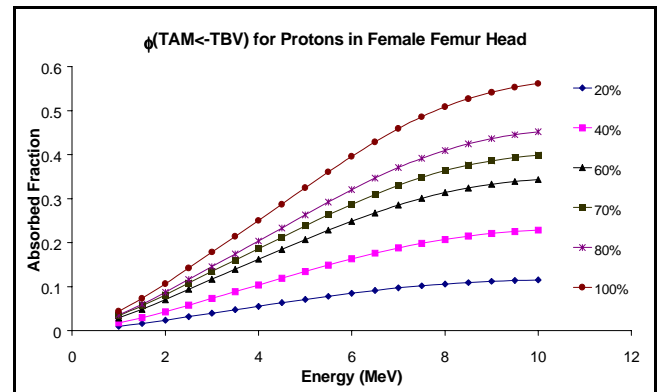


Fig. 26. Absorbed fraction to TAM in male humeral epiphysis for protons from a TBV source with varying cellularity.

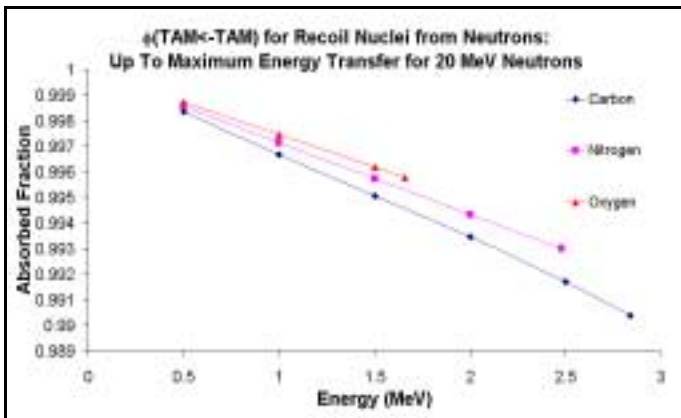


Fig. 27. Absorbed fraction for different recoil nuclei resulting from neutron interactions. The maximum energy is taken for an interaction of the nuclei with a 20 MeV neutron.

10. Improved Characterization of the Bone-Marrow Interface for Radiation Dosimetry Modeling

As discussed in Section 2, dosimetry errors can occur in transporting short-ranged particles within voxelized representations of trabecular bone. In this task, we have explored improved methods of representing the bone-marrow interface so as to minimize these effects as much as possible. Fig. 28 shows a 3D representation of a sample of trabecular bone, below which is an enlarged section of a region of a single marrow cavity. In the lower figure, the bone-marrow interface is represented, not as individual voxels of bone, but has a grid of triangular segments using the Marching Cubes Algorithm, a technique originally developed for 3D visualization of digital objects (12, 13). Our research team is the first to apply this algorithm to a digital image needed as input to a radiation transport code (e.g., EGSnrc). As displayed in Fig. 29a, improvements are shown to be minimal for accurate measurements of the marrow volume fraction; however, substantial improvements in measurements of the trabecular surface area are shown in Fig. 29b. The voxelized model approaches a 50% overestimate of the trabecular surfaces, a fact that does not change with increasing higher resolution. For the MC model, errors of only a few percent are found at voxel sizes of ~50-60 μm , that achievable via NMR microscopy. The corresponding improvements in electron dosimetry are noted in Figs. 28 and 29. In Fig. 28, the relative error in the cross-region absorbed fraction (a- marrow source irradiating bone, or b – bone source irradiating marrow), are shown to approach 35% for 50-keV electrons. For the surface-smoothed model, however, errors of only a few percent are approached at voxel sizes below ~60 μm for all electron source energies (see Fig 29).

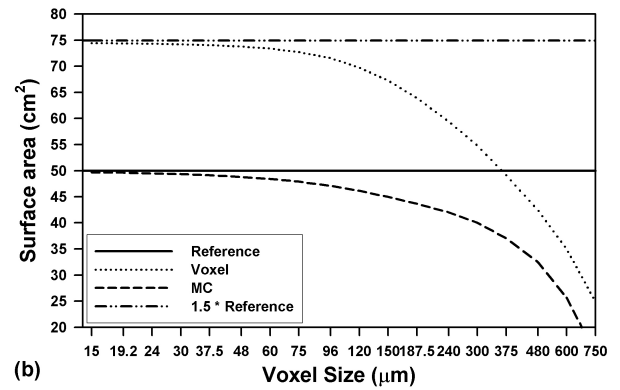
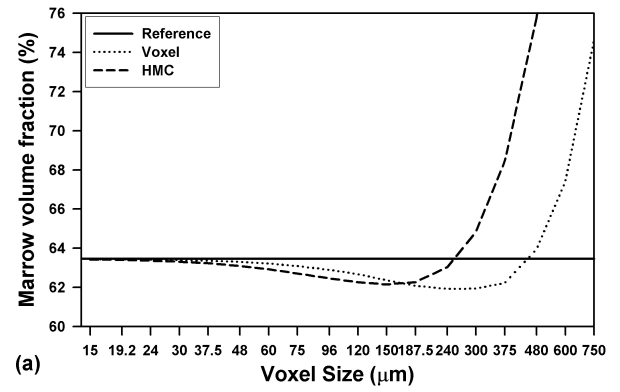
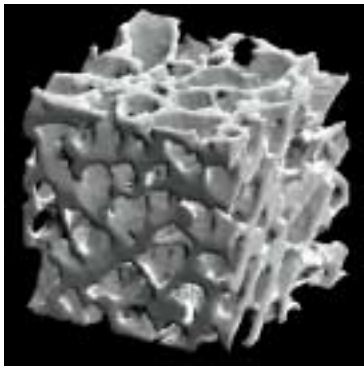


Fig. 28. 3D representation of a sample of trabecular bone. The bottom figure shows a small segment of the bone trabecular in which the bone-marrow interface is approximated using the Marching Cube algorithm.

Fig. 29. Comparison of both (a) marrow volume fraction and (b) bone-marrow interface surface area as a function of voxel size using the voxel representation of the sample, and that which is surface-smoothed via the Marching Cubes algorithm.

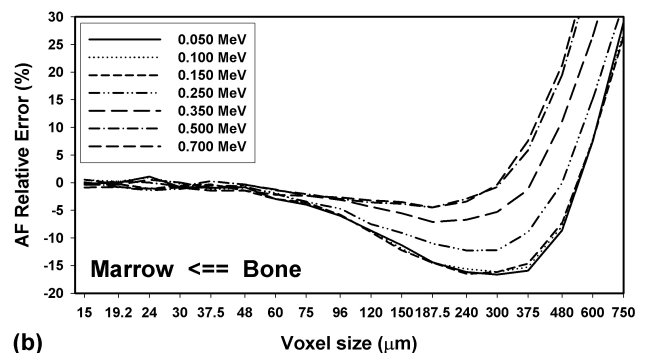
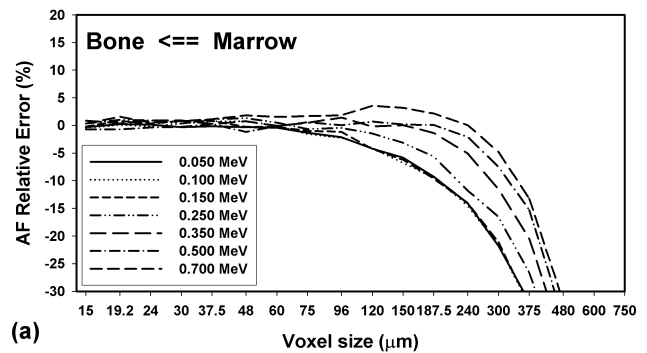
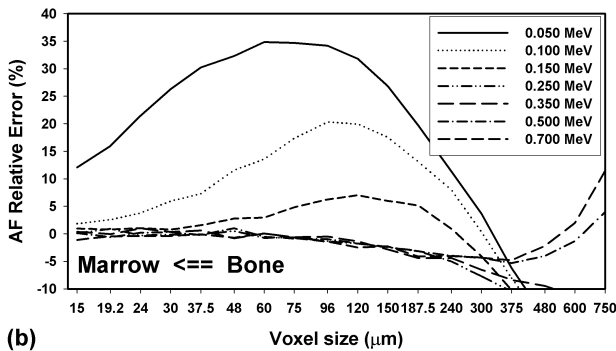
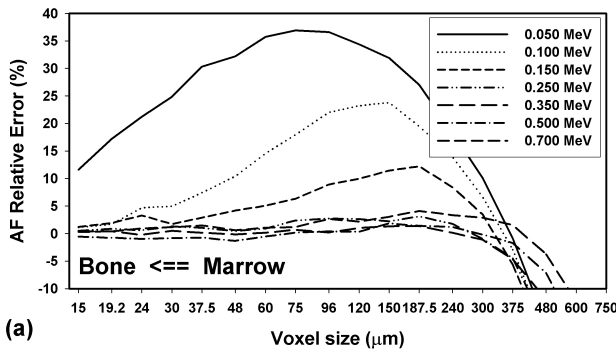


Fig. 28. Relative errors in monoenergetic electron absorbed fractions for the voxelized model of trabecular bone.

Fig. 29. Relative errors in monoenergetic electron absorbed fractions for the surface-smoothed model of trabecular bone.

Publications (Published or In Press)

Notes: The senior author(s) - underlined, Corresponding Author - **bold**, Graduate students of Dr. Bolch - **asterisk**

1. LG Bouchet^{*}, DW Jokisch^{*}, **WE Bolch**, "A Three-Dimensional Transport Model for Determining Absorbed Fractions of Energy for Electrons within Trabecular Bone" *J. Nucl. Med.* **40** (11): 1947-1966 (1999).
2. LG Bouchet^{*}, **WE Bolch**, "A Three-Dimensional Transport Model for Determining Absorbed Fractions of Energy for Electrons within Cortical Bone" *J. Nucl. Med.* **40** (12): 2115-2124 (1999).
3. LG Bouchet^{*}, **WE Bolch**, RW Howell, and **DV Rao**, "S Values for Radionuclides Localized within the Skeleton", *J. Nucl. Med.* **41** (1): 189-212 (2000).
4. LG Bouchet^{*}, **WE Bolch**, SM Goddu, RW Howell, and **DV Rao**, "Considerations in the selection of radiopharmaceuticals for palliation of bone pain from metastatic osseous lesions", *J. Nucl. Med.* **41** (4): 682-687 (2000).
5. SM Goddu, Bishayee, A., LG Bouchet^{*}, **WE Bolch**, DV Rao, and **RW Howell**, "Marrow toxicity of P-33 versus P-32 orthophosphate: implications for therapy of bone pain and bone metastases" *J. Nucl. Med.* **41** (41): 941-951 (2000).
6. A Bishayee, DV Rao, SC Srivastava, LG Bouchet^{*}, **WE Bolch**, and **RW Howell**, "Marrow-sparing effects of Sn-117m(4+) DTPA for radionuclide therapy of the skeleton" *J. Nucl. Med.* **41** (12): 2043-2050 (2000).
7. DA Rajon^{*}, DW Jokisch, PW Patton^{*}, AP Shah^{*}, and **WE Bolch**, "Voxel size effects in 3D NMR microscopy performed for trabecular bone dosimetry" *Med. Phys.* **27** (11): 2624-2635 (2000).
8. DW Jokisch^{*}, LG Bouchet, PW Patton^{*}, DA Rajon^{*}, and **WE Bolch**, "Beta-particle dosimetry of the trabecular skeleton using Monte Carlo transport in 3D digital images" *Med. Phys.* **28** (7): 1505-1518 (2001).
9. DW Jokisch^{*}, PW Patton^{*}, DA Rajon^{*}, BA Inglis, and **WE Bolch**, "Chord distributions across 3D digital images of a human thoracic vertebra" *Med. Phys.* **28** (7): 1493-1504 (2001).
10. **WE Bolch**, "Alpha-particle emitters in radioimmunotherapy: New and welcomed challenges to medical internal dosimetry" *J. Nucl. Med.* **42** (8): 1222-1224 (2001).
11. PW Patton^{*}, DA Rajon^{*}, AP Shah^{*}, DW Jokisch, BA Inglis, **WE Bolch**, "Site-specific variability in trabecular bone dosimetry: considerations of energy loss to cortical bone." *Med Phys* **29**(1): 6-14 (2002).
12. B Aydogan^{*}, DT Marshall, SG Swarts, JE Turner, AJ Boone, NG Richards, and **WE Bolch**, "Site-specific OH attack to the sugar moiety of DNA: A comparison of experimental data and computational simulation" *Radiat Res* **157** (1): 38-44 (2002).
13. **WE Bolch**, PW Patton^{*}, DA Rajon^{*}, AP Shah^{*}, DW Jokisch, and BA Inglis, "Considerations of marrow cellularity in 3D dosimetric models of the trabecular skeleton" *J Nucl Med* **43**(1) 97-108 (2002).
14. PW Patton^{*}, DW Jokisch, DA Rajon^{*}, AP Shah^{*}, BA Inglis, SL Myers, and **WE Bolch**, "Skeletal dosimetry via NMR microscopy: Investigations of sample reproducibility and signal source" *Health Phys* **82** (3): 316-326 (2002)
15. DA Rajon^{*}, PW Patton, AP Shah^{*}, CJ Watchman^{*}, and **WE Bolch**, "Surface area overestimation within 3D digital images and its consequences for skeletal dosimetry" *Med Phys* **29** (5): 682- 693 (2002).
16. DA Rajon^{*}, DW Jokisch, PW Patton, AP Shah^{*}, CJ Watchman^{*}, and **WE Bolch**, "Voxel effects within digital images of trabecular bone and their consequences on chord length distribution measurements" *Phys Med Biol* **47**: 1741-1759 (2002).
17. **WE Bolch**, PW Patton^{*}, AP Shah^{*}, DA Rajon^{*}, and DW Jokisch, "Considerations of anthropometric, tissue volume, and tissue mass scaling for improved patient specificity of radionuclide S values in the skeleton." *Med Phys* **29** (6): 1054-1070 (2002).
18. **MG Stabin**, KF Eckerman, **WE Bolch**, LG Bouchet, and PW Patton, "Evolution and status of bone and marrow dose models" *Cancer Biotherapy and Radiopharmaceuticals* **17**(4): 427-434 (2002).
19. DA Rajon^{*} and **WE Bolch**, "Interactions with 3D isotropic and homogeneous radiation fields: A Monte Carlo simulation algorithm" *Comput Methods Programs Biomed* (in press)

Publications (Submitted or In Review)

20. DA Rajon^{*}, AP Shah^{*}, CJ Watchman^{*}, JM Brindle^{*}, and **WE Bolch**, "A hyperboloid representation of the bone-marrow interface within 3D NMR images of trabecular bone: Applications to skeletal dosimetry" (submitted *Phys Med Biol*).
21. DA Rajon^{*} and **WE Bolch**, "Marching Cubes algorithm: Review and trilinear interpolation adaptation for image-based dosimetric models" (submitted to *Comput Med Imag Graph*)
22. AP Shah^{*}, PW Patton, DA Rajon^{*}, and **WE Bolch**, "Adipocyte spatial distributions in bone marrow: Implications for skeletal dosimetry models" (submitted to *J Nucl Med*)

Abstracts Presented at International Scientific Meetings

1. WE Bolch "Skeletal Dosimetry Through NMR Microscopy", 2nd International Workshop on Anatomic Models, Oak Ridge, Tennessee, September 28-30, 1999.
2. WE Bolch "Anatomic Models: The MIRD Perspective", 2nd International Workshop on Anatomic Models, Oak Ridge, Tennessee, September 28-30, 1999.
3. DA Rajon*, DW Jokisch*, PW Patton*, AP Shah*, and WE Bolch, "3D NMR Microscopy in Skeletal Dosimetry: A Study of Voxel Size Effects on Dose Estimates", World Congress on Medical Physics and Biomedical Engineering, Chicago, Illinois, July 23-28, 2000. [Supplement to *Med. Phys.* **27** (6) 1432, June 2000]
4. WE Bolch, PW Patton, AP Shah, DA Rajon, and DW Jokisch. "An assessment of anthropometric parameters for scaling radiation dose estimates to active marrow", 7th International Radiopharmaceutical Dosimetry Symposium, Nashville, Tennessee, April 17-19, 2002.

Abstracts Presented at National Scientific Meetings

1. LG Bouchet* and WE Bolch, "New Estimates of Specific Effective Energy for Use in Skeletal Dosimetry", 44th Annual Meeting of the Health Physics Society, Philadelphia, Pennsylvania, June 27 - July 1, 1999. [Supplement to *Health Phys.* **76** (6) S161-S162, 1999].
2. DW Jokisch*, PW Patton*, LG Bouchet*, and WE Bolch, "Monte Carlo Electron Transport within Voxels from a Three-Dimensional Image of Human Trabecular Bone", 44th Annual Meeting of the Health Physics Society, Philadelphia, Pennsylvania, June 27 - July 1, 1999. [Supplement to *Health Phys.* **76** (6) S161, 1999].
3. DA Rajon*, DW Jokisch*, PW Patton*, LG Bouchet*, and WE Bolch, "Assessment of Minimum Voxel Size for Trabecular Bone NMR Imaging for Dosimetry Calculations", 44th Annual Meeting of the Health Physics Society, Philadelphia, Pennsylvania, June 27 - July 1, 1999. [Supplement to *Health Phys.* **76** (6) S161, 1999].
4. PW Patton*, DW Jokisch*, DA Rajon*, EJ Eschbach, DL Wheeler, SL Myers, and WE Bolch, "Comparison of Trabecular Chord Length Distributions Obtained from Nuclear Magnetic Resonance Imaging and Optical Microscopy", 44th Annual Meeting of the Health Physics Society, Philadelphia, Pennsylvania, June 27 - July 1, 1999 [Supplement to *Health Phys.* **76** (6) S120, 1999].
5. DW Jokisch, PW Patton*, DA Rajon*, A Shah*, and WE Bolch, "The Effects Of The Bone-Marrow Interface In Trabecular Bone Dosimetry of Beta-Particles Utilizing Voxel-Based Transport", 45th Annual Meeting of the Health Physics Society, Denver, Colorado, June 25-29, 2000. [Supplement to *Health Phys.* **78** (6) S121 (2000)].
6. PW Patton*, DW Jokisch, DA Rajon*, A Shah*, and WE Bolch, "Introduction of Marrow Cellularity in 3D Electron Simulations in Trabecular Bone", 45th Annual Meeting of the Health Physics Society, Denver, Colorado, June 25-29, 2000. [Supplement to *Health Phys.* **78** (6) S98 (2000)].
7. DA Rajon*, PW Patton*, A Shah*, WE Bolch, "Surface Error Effects of 3D NMR Images on Monte Carlo Trabecular Bone Dosimetry Calculations", 45th Annual Meeting of the Health Physics Society, Denver, Colorado, June 25-29, 2000. [Supplement to *Health Phys.* **78** (6) S121 (2000)].
8. AP Shah*, PW Patton*, DW Jokisch, DA Rajon*, and WE Bolch, "Geometrical Distribution of Adipocytes within Normal Bone Marrow: Considerations for 3D Skeletal Dosimetry Models", 45th Annual Meeting of the Health Physics Society, Denver, Colorado, June 25-29, 2000. [Supplement to *Health Phys.* **78** (6) S100 (2000)].
9. LG Bouchet, I. Clairand*, WE Bolch, "Improvement of Skeletal Internal Dosimetry Associated with Photon Sources", 47th Annual Meeting of the Society of Nuclear Medicine, St. Louis, Missouri, June 3-7, 2000. [Supplement to *J. Nucl. Med.* **41** 237P (2000)].
10. LG Bouchet, I. Clairand*, WE Bolch, "Improvement of Skeletal Internal Dosimetry for Pediatric Patients", 47th Annual Meeting of the Society of Nuclear Medicine, St. Louis, Missouri, June 3-7, 2000. [Supplement to *J. Nucl. Med.* **41** 238P (2000)].
11. WE Bolch, DW Jokisch*, PW Patton*, DA Rajon*, and LG Bouchet, "Investigation of NMR Microscopy for Use in Skeletal Dosimetry Models", 47th Annual Meeting of the Society of Nuclear Medicine, St. Louis, Missouri, June 3-7, 2000. [Supplement to *J. Nucl. Med.* **41** 83P (2000)].
12. MG Stabin, KF Eckerman, WE Bolch, and LG Bouchet, "Consensus bone and marrow model for internal dose assessment", 48th Annual Meeting of the Society of Nuclear Medicine, Toronto, Ontario, Canada, June 23-27, 2001. [Supplement to *J. Nucl. Med.* **42** 244P (2001)]
13. BW Wessels, WE Bolch, HB Breitz, RF Meredith, RM Sharkey, and GL Denardo, "Bone marrow dosimetry for radionuclide therapy – A multi-institutional comparison", 48th Annual Meeting of the Society of Nuclear Medicine, Toronto, Ontario, Canada, June 23-27, 2001. [Supplement to *J. Nucl. Med.* **42** 22P (2001)]
14. DA Rajon*, DW Jokisch, PW Patton*, AP Shah*, CJ Watchman*, and WE Bolch, "Chord length distribution measurements through 3D NMR images of trabecular bone samples", 46th Annual Meeting of the Health Physics Society, Cleveland, Ohio, June 10-14, 2001. [Supplement to *Health Phys.* **80** (6) S127 (2001)]
15. AP Shah*, PW Patton*, DA Rajon*, and WE Bolch, "Geometrical variations in adipocyte distribution for skeletal dosimetry models: considerations for 3D electron simulations", 46th Annual Meeting of the Health Physics Society, Cleveland, Ohio, June 10-14, 2001. [Supplement to *Health Phys.* **80** (6) S127 (2001)].

16. CJ Watchman^{*}, DK Vo^{*}, DA Rajon^{*}, AP Shah^{*}, and WE Bolch, "Calculation of heavy charged particle absorbed fractions in trabecular bone", 46th Annual Meeting of the Health Physics Society, Cleveland, Ohio, June 10-14, 2001. [Supplement to *Health Phys.* **80** (6) S126 (2001)].
17. PW Patton^{*}, DA Rajon^{*}, DW Jokisch, AP Shah^{*}, and WE Bolch, "Trabecular bone dosimetry: the role of marrow cellularity and bone site variations", 43rd Annual Meeting of the American Association for Physicists in Medicine, July 22-26, 2001 Salt Lake City, Utah. [Supplement to *Medical Phys.* **28** (6) 1288 (2001)].
18. DA Rajon^{*}, AP Shah^{*}, CJ Watchman^{*}, JM Brindle^{*}, and WE Bolch, "Chord length distribution measurements through polygonal representations of trabecular bone samples", 2002 Annual Meeting of the Health Physics Society, Tampa, Florida, June 16-20, 2002 [Supplement to *Health Phys.* **82** (6) S128 (2001)].
19. D Rajon^{*}, A Shah^{*}, C Watchman^{*}, J Brindle^{*}, and W Bolch, "Polygonal representation of trabecular bone samples for chord length distribution measurements", 2002 Annual Meeting of the American Association of Medical Physicists, Montreal, Canada, July 14-18, 2002.

References

1. Jokisch DW, Bouchet LG, Patton PW, Rajon DA, Bolch WE. Beta-particle dosimetry of the trabecular skeleton using Monte Carlo transport within 3D digital images. *Med Phys* 2001; 28:1505-1518.
2. Rajon DA, Jokisch DW, Patton PW, Shah AP, Bolch WE. Voxel size effects in 3D NMR microscopy performed for trabecular bone dosimetry. *Med Phys* 2000; 27:2624-2635.
3. Rajon D. *Trabecular bone dosimetry: Assessment of Minimum Voxel Size for Nuclear Magnetic Resonance Imaging*. Thesis. Nuclear and Radiological Engineering. Gainesville, FL: University of Florida; 1999.
4. Patton PW, Jokisch DW, Rajon DA, Shah AP, Myers SL, Bolch WE. Skeletal dosimetry via NMR microscopy: investigations of sample reproducibility and signal source. *Health Phys* 2002; 82:316-326.
5. Bouchet LG, Bolch WE, Howell RW, Rao DV. S values for radionuclides localized within the skeleton. *J Nucl Med* 2000; 41:189-212.
6. Eckerman KF, Stabin MG. Electron absorbed fractions and dose conversion factors for marrow and bone by skeletal regions. *Health Phys* 2000; 78:199-214.
7. Bolch WE, Patton PW, Rajon DA, Shah AP, Jokisch DW, Inglis B. Considerations of marrow cellularity in 3D dosimetric models of the trabecular skeleton. *J Nucl Med* 2002; 43:97-108.
8. Shah AP, Patton PW, Rajon DA, Bolch WE. Adipocyte spatial distributions in bone marrow: Implications for skeletal dosimetry models. *J Nucl Med* submitted;
9. Patton PW, Rajon DA, Shah AP, Jokisch DW, Inglis B, Bolch WE. Site-specific variability in trabecular bone dosimetry: considerations of energy loss to cortical bone. *Med Phys* 2002; 29:6-14.
10. Bouchet LG, Jokisch DW, Bolch WE. A three-dimensional transport model for determining absorbed fractions of energy for electrons in trabecular bone. *J Nucl Med* 1999; 40:1947-1966.
11. Bolch WE, Patton PW, Shah AP, Rajon DA. Considerations of anthropomorphic, tissue volume, and tissue mass scaling for improved patient specificity of skeletal S values. *Med Phys* 2002; 29:1054-1070.
12. Rajon D, Bolch W. Marching cubes algorithm: Review and trilinear interpolation adaptation for image-based dosimetric models. *Comp Med Imag Graph* submitted;
13. Rajon DA, Shah AP, Watchman CJ, Brindle JA, Bolch WE. A hyperboloid representation of the bone-marrow interface within 3D NMR images of trabecule bone: Applications to skeletal dosimetry. *Phys Med Biol* submitted;